$WSe_{(2-x)}Te_x$ alloys grown by molecular beam epitaxy

2D Materials

PAPER

$WSe_{(2-x)}Te_x$ alloys grown by molecular beam epitaxy

Adam T Barton[1], Ruoyu Yue[1], Lee A Walsh[1,2], Guanyu Zhou[1], Christopher Cormier[1], Christopher M Smyth[1], Rafik Addou[1], Luigi Colombo[1], Robert M Wallace[1] and Christopher L Hinkle[1,3]

[1] University of Texas at Dallas, 800 W. Campbell Rd., Richardson 75080, TX, United States of America
[2] Tyndall National Institute, University College Cork, Lee Maltings, Prospect Row, Cork, Ireland
[3] Department of Electrical Engineering, University of Notre Dame, Notre Dame, IN, United States of America

E-mail: chinkle@nd.edu

RECEIVED 8 May 2019
REVISED 8 July 2019
ACCEPTED FOR PUBLICATION 18 July 2019
PUBLISHED 30 July 2019

Keywords: mixed chalcogen alloys, WSe_2, WTe_2, phase change, phase separation

Supplementary material for this article is available online

Abstract

The growth of $WSe_{(2-x)}Te_x$ alloys by molecular beam epitaxy has been demonstrated for the first time to investigate the phase transition from the semiconducting 2H phase to the semi-metallic 1T′ phase as a function of Te concentration. Up to 14% Te incorporation, stable alloys in the semiconducting 2H phase are achieved while above 79% Te incorporation, stable alloys in the semi-metallic 1T′ phase are obtained. Our results indicate the MBE-grown $WSe_{(2-x)}Te_x$ alloys exhibit a miscibility gap from 14% to 79% Te concentrations at a growth temperature of 250 °C, a temperature compatible with direct vertical back-end-of-line integration. This miscibility gap results in phase separation of two different alloys, both with different composition and crystal structure. While the alloying of small Te concentrations does indeed result in a desired reduction of the semiconducting bandgap, the phase separation above 14% Te incorporation prohibits bandgap tuning for a wider range of applications. These results highlight the competing energies and kinetics associated with producing uniform $WSe_{(2-x)}Te_x$ alloys.

Introduction

With the end of conventional silicon-based device innovation on the horizon and the explosion of research focusing on novel materials for next-generation memory and logic circuitry, 2D transition metal dichalcogenides (TMDs) have emerged as viable candidates for the next-generation of low-power devices due to their wide range of electronic properties and monolayer scalability [1–4]. Until recently, the majority of research has focused on the fundamental investigation of the electronic properties and device applications using large-area bulk crystals grown at high temperature over a long growth period [5–8]. These studies have provided valuable insight into the unique physical, electronic, and quantum properties of TMDs, which can be exploited for innovative sensors, transistors, and energy storage [9–13]. As these materials are developed further, the semiconductor industry continues to search for new ways to tune the electronic properties for optimized performance. One method currently being investigated is the phase-engineering of TMDs, which permits control over the band structure and is therefore a critical engineering challenge to overcome before commercially viable novel device applications based on TMDs can be realized [14].

TMDs with a bandgap below 1 eV are of interest for prospective applications, in particular, for tunnel-field-effect-transistors (TFETs), where a sub-60 mV/dec subthreshold swing can be achieved without the fundamental switching constraints of thermionic emission [15, 16]. However, low on-currents remain a significant issue for TFET devices and bandgap engineering must be optimized to enhance the on-state current. Of course, the probability of tunneling between source and drain regions can be amplified by reducing the bandgap of the semiconducting TMD in the device [17–19], which can possibly be achieved by strategically forming ternary alloys. Alloying for band gap tuning has been successfully demonstrated in III–V materials such as $In_xGa_{1-x}As$ and $GaAs_xP_{1-x}$ alloys, but interfacial defects and alloy scattering have resulted in significant challenges [20–22]. In recent years, mixed-chalcogen or mixed-metal TMDs have been synthesized using a number of

deposition methods, usually at high growth temperatures (>800 °C) where the Gibbs free energy of mixing ($\Delta G_{mix} = \Delta H_{mix} - T\Delta S_{mix}$) is dominated by the entropy (ΔS) rather than the enthalpy (ΔH) of mixing. Specifically, wide bandgap semiconductors based on group VIB transitional metals (Mo and W) have been the focus of many previous reports. Both mixed-metal TMD alloys (i.e. $Mo_xW_{1-x}S_2$ or $Mo_xW_{1-x}Se_2$) [23–25] and mixed-chalcogen TMD alloys (i.e. MoS_xSe_{1-x}) have been investigated [26–28], where the bandgap varies by a few hundred meV over the stable composition range of each alloy.

A recent study performed by Yu *et al* demonstrated bandgap control of 2H-$WSe_{(2-x)}Te_x$ monolayers between 1.67 eV and 1.44 eV over the stable composition range up to 50% Te incorporation. However, alloys with a Te concentration greater than 50% exhibited phase separation into a semi-metallic 1T′ phase and a semiconducting 2H phase [31]. These results are somewhat promising for bandgap engineering, but a bandgap below 1 eV has not yet been achieved, limiting their applicability in TFET applications. Furthermore, the chemical vapor transport (CVT) growth technique required extremely long growth periods and high growth temperatures (~900 °C), which limits the range of potential applications due to typical thermal restrictions of the substrate or back-end-of-line circuitry. Conversely, very few studies investigating the crystal formation of thin-film TMD alloys have employed molecular beam epitaxy, where the much lower growth temperatures potentially enable direct integration of these TMD alloys into the back-end-of-line. MBE provides a number of advantages to closely investigate the growth of $WSe_{(2-x)}Te_x$ alloys, including the ultra-high vacuum deposition environment, low growth temperatures, high purity sources, and precise control of the elemental beam flux. These advantages allow for controlled deposition that can enable layer-by-layer thickness control directly on the substrate, even down to the monolayer.

2H–WSe_2 is a semiconductor that possesses trigonal prismatic coordination and a direct band gap of 2.4 eV in the monolayer form and an indirect bandgap of 1.4 eV in bulk. Although it has been well established that WTe_2 stabilizes in the distorted octahedral (1T′) phase and possesses semi-metallic properties [29], a recent theoretical study has predicted a 0.63 eV bandgap in the monolayer form of WTe_2 in the metastable 2H phase [30]. These results suggest a potential route for obtaining a semiconducting TMD with a sub-1 eV bandgap when alloying WTe_2 with Se. Figures 1(a) and (c) shows the chalcogen-metal coordination and (0 1 0) side view of 2H–WSe_2, respectively, where the uniform bond lengths result in a middle layer with uniform W spacing. Figures 1(b) and (d) shows the 1T′ phase of WTe_2, where the distorted structure results in W–W distances of 2.86 Å and 4.4 Å. This atomic coordination of WTe_2 produces an electronic structure where the valence and conduction bands exhibit a 0.3 eV overlap, forming the semi-metal.

Experimental details

The growth of $WSe_{(2-x)}Te_x$ presented in this research was performed in a VG-Semicon V80H MBE system equipped with an *in situ* reflection high-energy electron diffraction (RHEED) tool for real-time surface analysis [32]. A single-filament Knudsen effusion cell (*k*-cell) was used for selenium evaporation, a dual-filament, thermal cracker was utilized for tellurium evaporation, and a vertical *e*-beam evaporator was used for tungsten deposition. The $WSe_{(2-x)}Te_x$ films were grown directly on highly-oriented pyrolytic graphite (HOPG), CVT-grown MoS_2, and Bi_2Se_3 grown by MBE on sapphire (0 0 0 1) at a growth temperature of 250 °C. A nude ion gauge positioned at the focal point of deposition measured the chalcogen fluxes, while the W beam flux was calculated using blanket depositions and thickness measurements. A systematic increase in Te concentration of the alloys was achieved by keeping the flux pressures of Te and W constant at 8×10^{-7} mbar and 4×10^{-9} mbar, respectively, while incrementally reducing the Se flux pressure from 1×10^{-8} mbar to 1×10^{-9} mbar. The pure WSe_2 and WTe_2 reference samples were also grown at 250 °C using only the primary chalcogen flux, which was maintained at flux pressures of 6×10^{-8} mbar and 8×10^{-7} mbar, respectively. Prior to deposition, the HOPG and MoS_2 substrates were exfoliated immediately before loading into the UHV system and annealed to 400 °C for one hour, providing a clean surface free of environmental contaminants and oxidation [33, 34]. The Bi_2Se_3 substrates were grown on sapphire (0 0 0 1) using a two-step growth method at 320 °C (the growth details can be found in previous publications) [35, 36]. All heaters (*k*-cell, *e*-beam, and substrate) were maintained at the growth temperature for two hours to allow ample time for outgassing and temperature stabilization. To initiate growth, the elemental source shutters were opened simultaneously, and throughout the duration of the deposition, a beam-interruption growth technique was utilized for the W flux, where the shutter was cycled between open and closed for 30 s and 90 s, respectively. Due to the slow growth rate of the beam interrupted films, a six hour growth period was needed to form a film ~3 nm thick (four monolayers). More information on the preparation of the substrates and the effectiveness of beam-interrupted growth for WSe_2 and WTe_2 can be found in previous publications [37, 38].

X-ray photoelectron spectroscopy (XPS) measurements, including valence band spectra, were carried out using a monochromated Al Kα source and an Omicron EA125 hemispherical analyzer with a spectral resolution of ±0.05 eV. An analyzer acceptance angle of 8°, takeoff angle of 45°, and pass energy

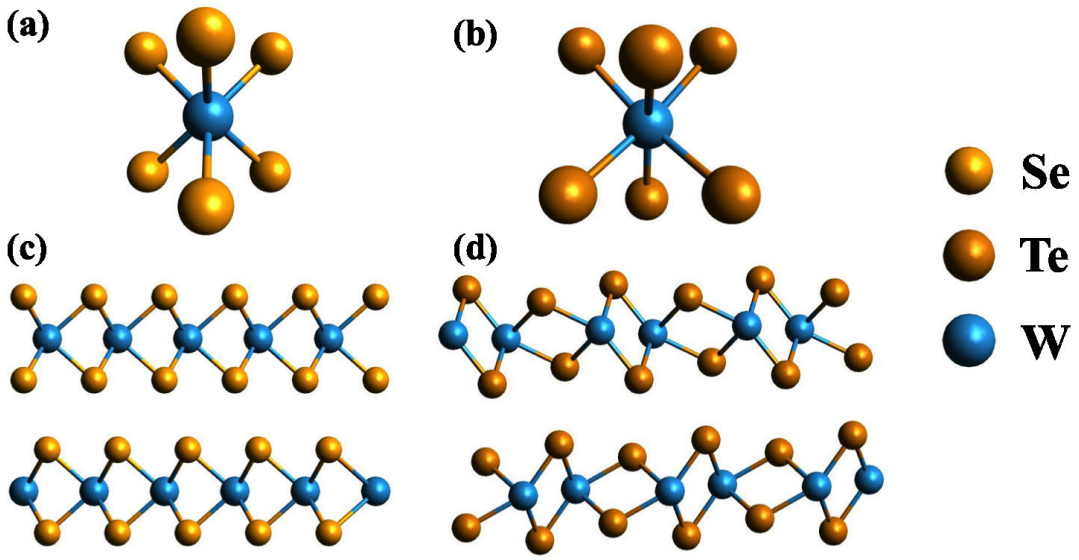

Figure 1. Ball and stick models showing (a) the trigonal prismatic coordination of 2H–WSe_2 and (b) the distorted octahedral coordination of 1T′-WTe_2. Cross-section view of bilayer (c) 2H–WSe_2 and (d) 1T′-WTe_2.

of 15 eV were used in this study. Additional information about the XPS system can be found in previously published literature [39]. The integrated intensities of relevant chemical states in the XPS core level spectra were used to calculate the stoichiometry of the films using the appropriate relative sensitivity factors for the W 4*f*, Te 4*d*, and Se 3*d* core levels (2.959, 1.388, 0.722, respectively). The core levels were deconvoluted using version 1.36 of the curve-fitting software AAnalyzer [40]. An active Shirley-Sherwood background was subtracted when fitting all spectra. Metallic chemical states were fit using an asymmetric double-Lorentzian line shape, while non-metallic chemical states were fit with Voigt (symmetric) line shapes [41]. Low-energy electron diffraction (LEED) patterns and scanning tunneling microscopy/spectroscopy (STM/S) were acquired in a separate Omicron tool from where the XPS was measured. LEED and RHEED used bare MoS_2 and Bi_2Se_3 patterns for reference. Raman spectra were acquired using an average of 20 sweeps where a Renishaw confocal Raman system was employed with an excitation wavelength of 532 nm, laser power of 0.22 mW, and spot size of 500 nm.

Results and discussion

Due to the relatively low growth temperature employed in MBE, both the kinetics of the atoms on the substrate and thermodynamics of the crystal formation must be considered when optimizing a deposition process. The sticking coefficient of elemental beam fluxes decreases and the desorption coefficient increases with increasing substrate temperature [42]. Generally speaking, this results in a decreased nucleation rate at higher substrate temperatures. Furthermore, by raising the temperature of the substrate, the probability of bond scission and forming more thermodynamically favorable crystals is improved.

A previous report [37] showed the MBE growth of WTe_2 involves a dominant density of Te_2 dimers in the deposition beam flux (~95%), which required the use of an extremely high Te:W flux pressure ratio (200:1) along with a periodically interrupted W flux to produce stoichiometric WTe_2 films due to the low flux density of atomic Te. Although the density of Te_2 dimers can be reduced with the use of a high-temperature cracking region, they still present a significant kinetic challenge when growing Te-based crystals at substrate temperatures below the thermal energy threshold needed to dissociate Te–Te dimers on the surface (259.8 ± 5 kJ/mol) [43]. Se_6 clusters are the dominant species in the Se vapor phase (~47%), but they do not detrimentally dominate the atomic flux pressure like the Te_2 dimers [44]. This creates a growth condition that only requires a Se:W flux pressure ratio of 20:1 to produce stoichiometric WSe_2 in contrast with the extremely high Te:W flux pressure ratio required for stoichiometric WTe_2. This introduces an imbalance when growing $WSe_{(2-x)}Te_x$ alloys by saturating the substrate surface with Te_2 dimers that do not participate in the growth. Furthermore, the enthalpy of formation of W–Se is more energetically favorable than W–Te (185.3 ± 5.5 kJ/mol compared to 38 ± 5 kJ/mol, respectively) [45, 46], which further exacerbates the challenge of incorporating Te into mixed chalcogen alloys.

To investigate the evolution of the physical and electronic properties of $WSe_{(2-x)}Te_x$ alloys, a series of samples were grown with the Te concentration varying from 0% to 100%. Shown in figure 2, the valence band offset (VBO) for the WSe_2 reference film was determined to be ~0.66 eV and is consistent with a

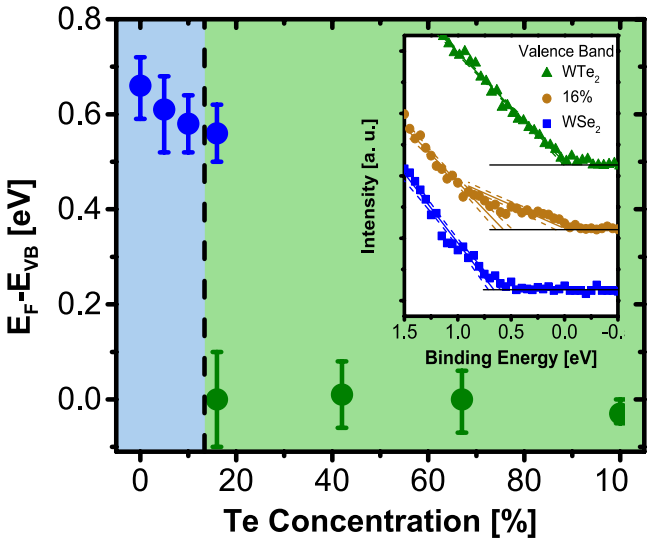

Figure 2. Plot of the VBO versus Te concentration over a wide range of $WSe_{(2-x)}Te_x$ alloys. The blue region represents alloys in the semiconducting 2H phase, and the green region represents alloys that exhibit metallic characteristics. The inset shows the valence band spectra of the two stoichiometric references along with the 16% Te alloy, where two stages of linear increase in intensity reflect both the semiconducting 2H alloy and the semi-metallic 1T′ alloy. The VBO and the 95th percentile confidence intervals to the linear regression that provided the VBO for the WSe_2, 16% Te film, and WTe_2 film, respectively, are (WSe_2: 0.66 eV, 0.72 eV, 0.59 eV, 16%Te: 0.56 eV, 0.62 eV, 0.50 eV, WTe_2: −0.03 eV, 0.00 eV, −0.05 eV). These were obtained from a linear regression to the data, as shown.

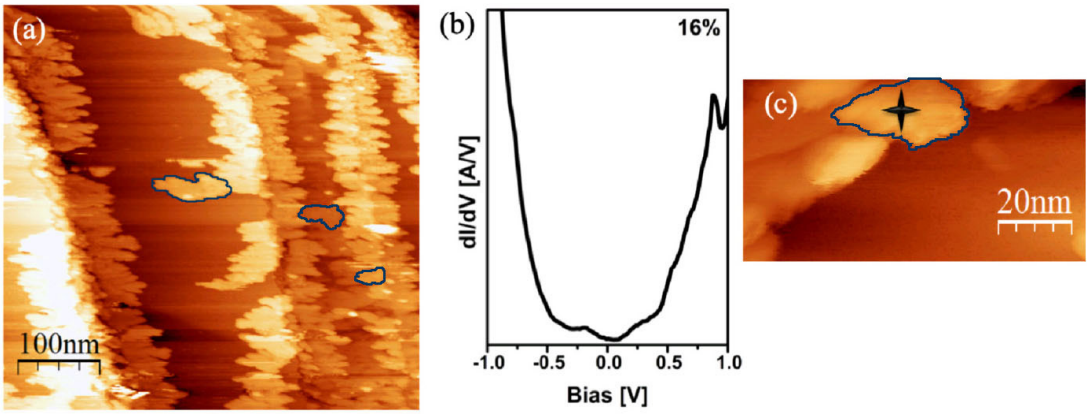

Figure 3. (a) Large-area STM image of sub-monolayer $WSe_{1.68}Te_{0.32}$/HOPG showing the initial nucleation occurring at the step edges of the HOPG substrate. Select grains are outlined as a guide to the reader. (b) STS data obtained from the same sample showing a measureable density of states near the Fermi level indicating the presence of the semi-metallic1 T′ phase. (c) Zoomed-in image where the star indicates the point from which the STS data was acquired.

near-midgap Fermi level in multilayer WSe_2 (band-gap ≅ 1.4 eV) [38]. Due the aforementioned vast differences in dissociation and formation energies, small amounts of Te were incorporated into the $WSe_{(2-x)}Te_x$ films only after significantly reducing the Se flux while maintaining a high Te flux. The VBO is concomitantly reduced to 0.61 eV and 0.58 eV in alloys containing 5% and 10% Te concentrations, respectively. However, the inset in figure 2 shows an appreciable density of states are generated at the Fermi level when the Te concentration is 16% in addition to the density of states detected away from the Fermi level associated with the valence band edge of semiconducting WSe_2. All Te concentrations higher than 16% (green region) exhibit $WSe_{(2-x)}Te_x$ alloys that begin to phase separate

Figure 3(a) shows an STM image of sub-monolayer $WSe_{1.68}Te_{0.32}$, where the initial nucleation along the HOPG step edges results in small grains tens of nanometers across. STS data obtained from the same sample (figure 3(b)) shows a DOS near the Fermi level, which is consistent with the XPS results (inset in figure 2).

Detailed XPS analysis of the Se 3*d*, Te 3*d*, and W 4*f* core level spectra was performed to investigate the evolution of the chemical states in the ternary alloys as a function of composition. In figure 4(a), a broad peak was detected in the Te 3*d* core level spectra at ~573.2 eV from each of the ternary alloys. This chemical state exhibits a higher BE than the chemical state detected in the Te 3*d* core level in the WTe_2 reference (labelled

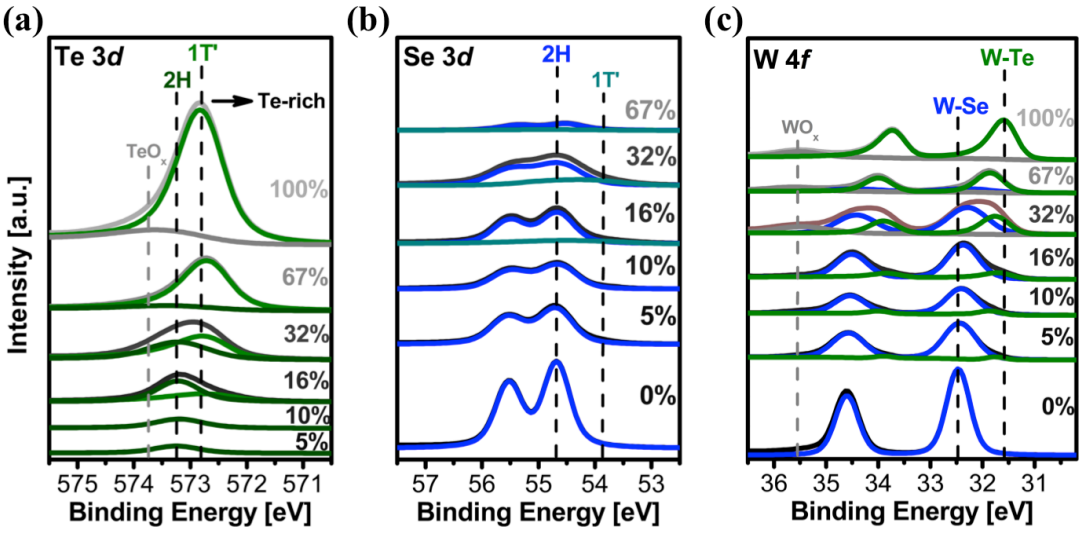

Figure 4. Deconvoluted XPS spectra of the WTe_xSe_{2-x} alloys for the (a) Te 3*d*, (b) Se 3*d*, and (c) W 4*f* core levels. At 16% Te concentration, phase separation is observed by the appearance of both metallic and non-metallic features in the Te 3*d*, Se 3*d*, and W 4*f* core levels. The phase separation persists at all compositions up to and including the 67% total composition.

100%) and indicates the presence of an alloy in the semiconducting 2H phase. Furthermore, as the Te concentration is increased to 16%, a second, asymmetric feature at lower binding energy was deconvolved from the corresponding Te 3*d* spectra. The asymmetric double Lorentzian line shape and lower BE indicates the presence of a Te-rich, metallic-like state, which is consistent with the semi-metallic 1T′ phase as also detected in the corresponding valence band spectra. Thus, we attribute this peak to the formation of a 1T′ phase alloy.

The Te 3*d* core level can be used to calculate the miscibility gap of these films. Using the intensities of the 1T′ and 2H chemical states from the 16%, 32%, and 67% Te concentration samples using a self-consistent fitting procedure, the binding energy of the 1T′ and 2H phases are stable at 572.75 eV and 573.40 eV, respectively. The concentration of the two phases in the Te 3*d* core level were employed to determined that the 1T′ phase is composed of 79% Te ($WSe_{0.42}Te_{1.58}$) and the 2H phase is composed of 14% Te ($WSe_{1.72}Te_{0.28}$). These stoichiometries represent the endpoints of the miscibility gap of these alloys at this growth temperature and indicates an energetically unfavorable enthalpy of mixing for $WSe_{(2-x)}Te_x$ alloys. Figure 4(b) shows the Se 3*d* core level spectra obtained from the range of alloys, where the emergence of an asymmetric feature at 16% Te indicates a small amount of Se is incorporated into the 1T′ crystal structure. The chemical state associated with the 2H crystal structure exhibits an increasing shift to lower binding energy as the total Te concentration increases, which is consistent with an increase in Te concentration in the 2H crystal structure.

The evolution of the tungsten chemical states (W–Se and W–Te bonding) as a function of Te concentration was evaluated using the W 4*f* core level, which is shown in figure 4(c). Two chemical states (W-Se and W-Te) were deconvolved from the '5%' and '10%' W 4*f* spectra, which were fit using symmetric Voigt line shapes indicating the chemical states correspond to semiconducting phases [40]. However, once the Te concentration reaches 16%, a chemical state with asymmetric line shape was detected indicating the presence of the semi-metallic, Te-rich 1T′-$WSe_{(2-x)}Te_x$ phase. The intensity of the chemical state associated with the 1T′ phase increases as the Te concentration is increased to 67%. The shift to higher binding energy from the WTe_2 reference exhibited by the W–Te chemical state in each of the W 4*f* core level spectra is likely due to final state electron density effects in metallic alloys [41]. Furthermore, the increase in the high binding energy WO_x chemical state in samples containing more than 16% Te concentration is consistent with an increased oxidation rate of Te rich films and is likely enhanced by the increased number of defects and grain boundaries with increasing Te concentration in the alloy (see supplementary information for more discussion of oxidation and surface contaminants in Te-rich films (stacks.iop.org/TDM/6/045027/mmedia)). These results obtained through careful analysis of the XPS core levels further support the early onset of phase separation in these low-temperature MBE-grown alloys and highlights a major engineering challenge that must be solved before $WSe_{(2-x)}Te_x$ alloys can be applied in novel device structures.

Due to the rapid oxidation of WTe_2 thin films, *ex situ* structural characterization of the as-grown alloys must be performed immediately after removing from UHV, while still considering the non-uniform oxidation rates between the Te-rich 1T′ phase and the Se-rich 2H phase. However, to avoid this issue, analysis of the surface using *in situ* RHEED can provide valuable insight into the phase separation of the $WSe_{(2-x)}Te_x$ alloys. Figure 5(c) shows an out-of-plane view of the atomic arrangement of the top layer of Se and W atoms

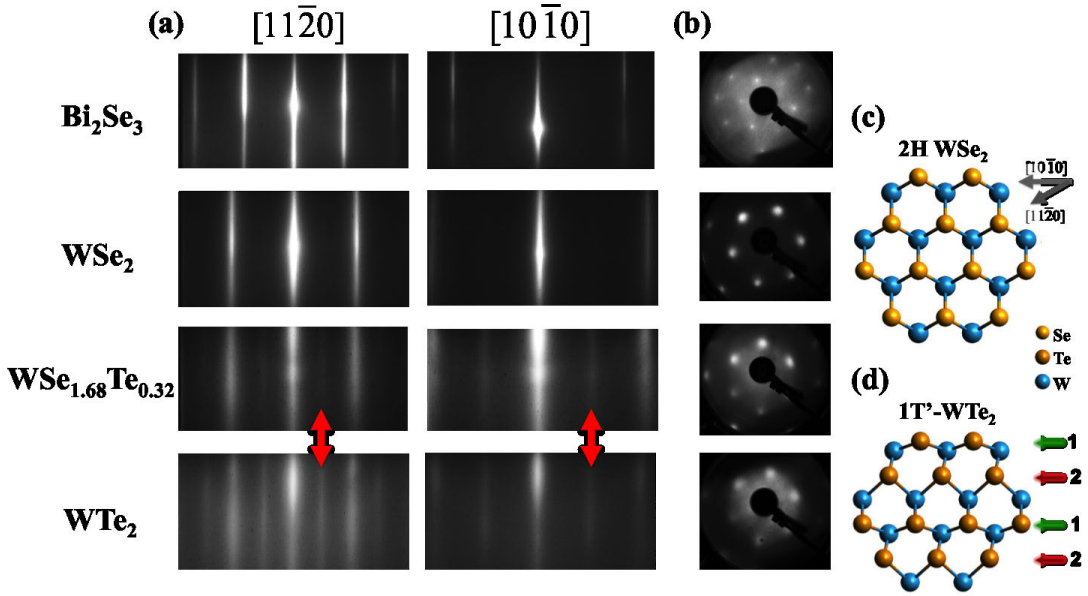

Figure 5. (a) RHEED patterns for the 1 1 $\bar{2}$ 0 and 1 0 $\bar{1}$ 0 directions with red arrows indicating the secondary set of streaks indicative of the 1T′ phase. (b) LEED pattern at 107.3 eV excitation energy. Ball and stick models for (c) 2H–WSe_2 and (d) 1T′-WTe_2 where the green and red arrows indicate alternating rows of top-surface Te atoms with varying out-of-plane displacements.

in the 2H phase. The trigonal prismatic coordination results in a 60° rotational symmetry along the surface where the two sets of evenly spaced Se atoms produce distinct RHEED patterns. Figure 5(d) shows the out-of-plane view of the upper layer of Se atoms along with the underlying W atoms of WTe_2 in the distorted 1T′ phase. The octahedral coordination of the unevenly spaced W atoms breaks the 60° surface symmetry of the 2H and 1T′ phases and results in alternating rows of Te atoms with out-of-plane displacements differing by 0.6 Å (indicated by the different color arrows in figure 5(d)). Although this change in crystal structure is significant enough to produce a distinctly different RHEED pattern (the additional streaks as highlighted with the red arrows in figure 5(a)), the symmetry still yields thin films in the 1T′ phase that are rotationally aligned to hexagonal substrates. The sharp spots observed in LEED patterns and the sharp streaks in the RHEED from pure WSe_2 fade to somewhat blurry spots and streaks in the 16% alloy and become even more blurry in those obtained from the WTe_2 reference (figure 5(b)). This is primarily due to the decrease in the average grain size as the Te content is increased as judged from the STM (see supplemental information). In fact, the grain size in the Te-rich films and pure WTe_2 is on the order of, or slightly larger than, the LEED transfer length of 20 nm. Additionally, in the phase separated films, there are two sets of RHEED patterns simultaneously with different, but close, reciprocal lattice spacing (the phase separated alloys have relatively close lattice constants). This leads to an additional spread/blurriness in the RHEED streaks (convolution of two patterns).

By applying the principles of RHEED analysis, a direct comparison of the lattice spacing of the can be achieved though the relation $\frac{s_1}{s_2} = \frac{a_2}{a_1}$ when all other variables are kept constant. In this case, s_1 and s_2 represent the RHEED streak spacing and a_1 and a_2 represent the atomic spacing of WSe_2 and WTe_2 respectively. Figures 5(a) and (b) shows a comparison of the RHEED and LEED patterns produced by the Bi_2Se_3/sapphire(0 0 0 1) substrate, 2H-WSe_2, 1T′-WTe_2, and the phase-separated $WSe_{(2-x)}Te_x$ alloy with 16% Te concentration. Using the method just described for directly comparing the diffraction patterns, both the RHEED and LEED pattern ratios fall within 2% of the expected ratio for WSe_2 and WTe_2 with lattice constants of 3.28 ± 0.02 Å and 3.49 ± 0.02 Å, respectively. The additional set of streaks (indicated by the red arrows) is again indicative of the 1T′ phase. The faint appearance of this additional set of streaks is further evidence of the emergence of the 1T′ phase in the alloy with 16% Te concentration.

Finally, to confirm the phase separation of the $WSe_{(2-x)}Te_x$ alloys, Raman spectra were acquired from $WSe_{(2-x)}Te_x$ samples with each of the Te concentrations (figure 6). One broad feature was detected from stoichiometric WSe_2 at ~250 cm^{-1} (overlapping in-plane E^1_{2g} and out-of-plane A_{1g} modes) and a second peak was detected at ~260 cm^{-1} (second order resonant Raman mode), which are consistent with previous reports of WSe_2 in the 2H phase [47, 48]. Incorporation of Te in the alloys resulted in a red-shift of the E^1_{2g} peak, which can be attributed to the high-frequency vibration caused by heavy Te atoms in the alloys. A significant reduction in peak signal to noise ratio was detected as the Te concentration was increased up to 32%, indicating a film with suppressed long-range order. Although the behavior of the WSe_2 Raman modes are consistent with the conclusions

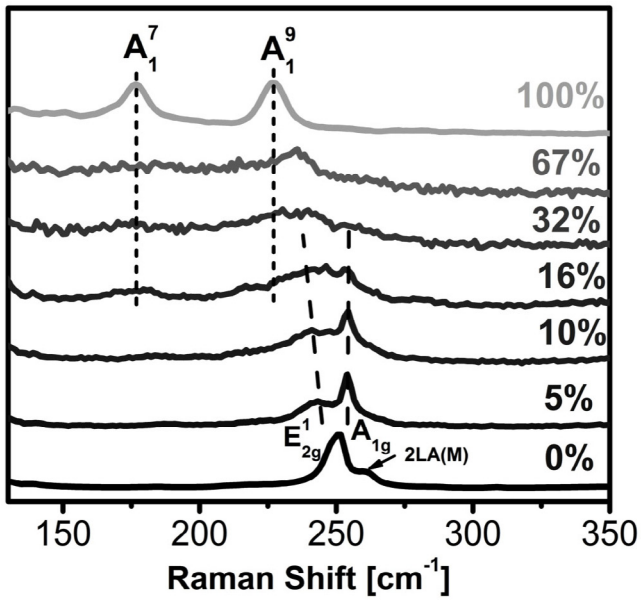

Figure 6. Raman spectra of the $WSe_{(2-x)}Te_x$ alloys showing a redshift of the 2H phase E^1_{2g} peak as a function of increasing Te concentration, and the onset of the 1T′ phase peaks.

drawn from the XPS results, the rapid oxidation of W atoms bonded to Te along with the *ex situ* exposure time needed to attain the Raman spectra (>15 min) makes it difficult to draw absolute conclusions regarding the magnitude of the phase separation. Despite the uncertainty in the absolute magnitude of the phase separation, the broad features detected in the spectra obtained from the films with 16% and 32% Te concentration around 230 cm^{-1} suggest the presence of the A_1^9 Raman mode exhibited by WTe_2. Two distinct peaks are detected at 170 cm^{-1} and 220 cm^{-1} in the Raman spectrum obtained from stoichiometric WTe_2 (corresponding to the A_1^7 and A_1^9 modes, respectively), which are consistent with a previous report and indicates the low density of defects in the stoichiometric film facilitates a greater oxidation resistance [49].

Conclusion

In conclusion, we have demonstrated the growth of $WSe_{(2-x)}Te_x$ alloys on van der Waals substrates by MBE and observed crystalline phase separation at Te concentrations much lower than previously reported in bulk alloys grown at much higher temperatures by CVT. *In situ* RHEED analysis in conjunction with *ex situ* XPS and Raman measurements indicate $WSe_{(2-x)}Te_x$ alloys remain stable in the semiconducting 2H phase until a concentration of ~14% Te is reached, at which composition phase separation results in the coexistence of a semiconducting 2H alloy and a semi-metallic 1T′ alloy. Alloys containing 79% Te are more stable in the 1T′ phase only. The edge of the miscibility gap at 14% is supported by patches of semi-metallic behavior detected by STS in regions of a sub-monolayer film with 16% Te concentration. The results presented in this research highlight the challenges facing the direct synthesis of $WSe_{(2-x)}Te_x$ thin film alloys in growth conditions compatible with the strict requirements associated with back-end-of-line semiconductor device processing where these alloys would be most useful.

Acknowledgments

This work was supported in part by NEWLIMITS, a center in nCORE, a Semiconductor Research Corporation (SRC) program sponsored by NIST through award number 70NANB17H041. This work was also supported in part by the National Science Foundation (NSF) through ECCS award numbers 1917025 and 1802166.

ORCID iDs

Lee A Walsh https://orcid.org/0000-0002-6688-8626
Guanyu Zhou https://orcid.org/0000-0002-2291-9427
Rafik Addou https://orcid.org/0000-0002-5454-0315
Robert M Wallace https://orcid.org/0000-0001-5566-4806
Christopher L Hinkle https://orcid.org/0000-0002-5485-6600

References

[1] Manzeli S, Ovchinnikov D, Pasquier D, Yazyev O V and Kis A 2017 2D transition metal dichalcogenides *Nat. Rev. Mater.* **2** 17033
[2] Mak K F and Shan J 2016 Photonics and optoelectronics of 2D semiconductor transition metal dichalcogenides *Nat. Photon.* **10** 216–26

[3] Kang K, Xie S, Huang L, Han Y, Huang P Y, Mak K F, Kim C J, Muller D and Park J 2015 High-mobility three-atom-thick semiconducting films with wafer-scale homogeneity *Nature* **520** 656–60

[4] Wang Q H, Kalantar-Zadeh K, Kis A, Coleman J N and Strano M S 2012 Electronics and optoelectronics of two-dimensional transition metal dichalcogenides *Nat. Nanotechnol.* **7** 699–712

[5] Xia J *et al* 2014 CVD synthesis of large-area, highly crystalline $MoSe_2$ atomic layers on diverse substrates and application to photodetectors *Nanoscale* **6** 8949

[6] Naylor C H *et al* 2016 Monolayer single-crystal 1T′-$MoTe_2$ grown by chemical vapor deposition exhibits weak antilocalization effect *Nano Lett.* **16** 4297–304

[7] McCreary K M, Hanbicki A T, Jernigan G G, Culbertson J C and Jonker B T 2016 Synthesis of large-area WS_2 monolayers with exceptional photoluminescence *Sci. Rep.* **6** 19159

[8] Schmidt H *et al* 2014 Transport properties of monolayer MoS_2 grown by chemical vapor deposition *Nano Lett.* **14** 1909–13

[9] Huang C, Wu S, Sanchez A M, Peters J J P, Beanland R, Ross J S, Rivera P, Yao W, Cobden D H and Xu X 2014 Lateral heterojunctions within monolayer $MoSe_2$–WSe_2 semiconductors *Nat. Mater.* **13** 1096–101

[10] Koppens F H L, Mueller T, Avouris P, Ferrari A C, Vitiello M S and Polini M 2014 Photodetectors based on graphene, other two-dimensional materials and hybrid systems *Nat. Nanotechnol.* **9** 780–93

[11] Ross J S *et al* 2014 Electrically tunable excitonic light-emitting diodes based on monolayer WSe_2 p–n junctions *Nat. Nanotechnol.* **9** 268–72

[12] Groenendijk D J *et al* 2014 Photovoltaic and photothermoelectric effect in a double-gated WSe_2 device *Nano Lett.* **14** 5846–52

[13] Wang Q, Lai J and Sun D 2016 Review of photo response in semiconductor transition metal dichalcogenides based photosensitive devices *Opt. Mater. Express* **6** 2313

[14] Voiry D, Mohite A and Chhowalla M 2015 Phase engineering of transition metal dichalcogenides *Chem. Soc. Rev.* **44** 2702–12

[15] Datta S, Liu H and Narayanan V 2014 Tunnel FET technology: a reliability perspective *Microelectron. Reliabil.* **54** 861–74

[16] Das S, Prakash A, Salazar R and Appenzeller J 2014 Toward low-power electronics: tunneling phenomena in transition metal dichalcogenides *ACS Nano* **8** 1681–9

[17] Khatami Y and Banerjee K 2009 Steep subthreshold slope n- and p-type tunnel-FET devices for low-power and energy-efficient digital circuits *IEEE Trans. Electron Devices* **56** 2752–61

[18] Sarkar D, Xie X, Liu W, Cao W, Kang J, Gong Y, Kraemer S, Ajayan P M and Banerjee K 2015 A subthermionic tunnel field-effect transistor with an atomically thin channel *Nature* **526** 91–5

[19] Ilatikhameneh H *et al* 2015 Tunnel field-effect transistors in 2D transition metal dichalcogenide materials *IEEE J. Exp. Solid-State Comput. Devices Circuits* **1** 12–18

[20] Stringfellow G B 2017 Thermodynamic considerations for epitaxial growth of III/V alloys *J. Cryst. Growth* **468** 11–6

[21] Bannow L C *et al* 2016 Configuration dependence of band-gap narrowing and localization in dilute GaAs alloys *Phys. Rev.* B **93** 205202

[22] Krijn M P C M 1991 Heterojunction band offsets and effective masses in III–V quaternary alloys *Semicond. Sci. Technol.* **6** 27–31

[23] Chen Y *et al* 2014 Composition-dependent Raman modes of $Mo_{1-x}W_xS_2$ monolayer alloys *Nanoscale* **6** 2833–9

[24] Zhang M *et al* 2014 Two-dimensional molybdenum tungsten diselenide alloys: photoluminescence, Raman scattering, and electrical transport *ACS Nano* **8** 7130–7

[25] Dumcenco D O, Kobayashi H, Liu Z, Huang Y-S and Suenaga K 2013 Visualization and quantification of transition metal atomic mixing in $Mo_{1-x}W_xS_2$ single layers *Nat. Commun.* **4** 1351

[26] Feng Q *et al* 2014 Growth of large-area 2D $MoS_{2(1-x)}Se_{2x}$ semiconductor alloys *Adv. Mater.* **26** 2648–53

[27] Li H *et al* 2014 Growth of alloy $MoS_{2x}Se_{2(1-x)}$ nanosheets with fully tunable chemical compositions and optical properties *J. Am. Chem. Soc.* **136** 3756–9

[28] Gong Y *et al* 2014 Band gap engineering and layer-by-layer mapping of selenium-doped molybdenum disulfide *Nano Lett.* **14** 442–9

[29] Augustin J *et al* 2000 Electronic band structure of the layered compound Td-WTe_2 *Phys. Rev.* B **62** 10812–23

[30] Lee C-H, Silva E C, Calderin L, Nguyen M A T, Hollander M J, Bersch B, Mallouk T E and Robinson J A 2015 Tungsten ditelluride: a layered semimetal *Sci. Rep.* **5** 10013

[31] Yu P *et al* 2016 Metal-semiconductor phase-transition in $WSe_{2(1-x)}Te_{2x}$ monolayer *Adv. Mater.* **29** 1603991

[32] Barton A T *et al* 2015 Transition metal dichalcogenide and hexagonal boron nitride heterostructures grown by molecular beam epitaxy *Microelectron. Eng.* **147** 306–9

[33] Walsh L A, Addou R, Wallace R M and Hinkle C L 2018 Molecular beam epitaxy of transition metal dichalcogenides *Molecular Beam Epitaxy: From Research to Mass Production* (Amsterdam: Elsevier) pp 515–53

[34] Pirkle A, Chan J, Venugopal A, Hinojos D, Magnuson C W, McDonnell S, Colombo L, Vogel E M, Ruoff R S and Wallace R M 2011 The effect of chemical residues on the physical and electrical properties of chemical vapor deposited graphene transferred to SiO_2 *Appl. Phys. Lett.* **99** 122108

[35] Ahn Y, Kim J, Ganorkar S, Kim Y-H and Kim S-I 2015 Thermal annealing of graphene to remove polymer residues *Mater. Express* **6** 69

[36] Walsh L A *et al* 2018 Fermi level manipulation through native doping in the topological insulator Bi_2Se_3 *ACS Nano* **12** 6310–8

[37] Walsh L A *et al* 2017 WTe_2 thin films grown by beam-interrupted molecular beam epitaxy *2D Mater.* **4** 025044

[38] Yue R *et al* 2017 Nucleation and growth of WSe_2: enabling large grain transition metal dichalcogenides *2D Mater.* **4** 045019

[39] Wallace R M 2008 *In situ* studies of interfacial bonding of high-*k* dielectrics for CMOS beyond 22 nm *ECS Trans.* **16** 255–71

[40] Herrera-Gómez A, Hegedus A and Meissner P L 2002 Chemical depth profile of ultrathin nitrided SiO_2 films *Appl. Phys. Lett.* **81** 1014–6

[41] Castellani N J and Leroy D B 1988 Final state core level binding energy shifts in binary alloys *Z. Phys.* B **71** 315–9

[42] Nie Y, Liang C, Cha P-R, Colombo L, Wallace R M and Cho K 2017 A kinetic Monte Carlo simulation method of van der Waals epitaxy for atomistic nucleation-growth processes of transition metal dichalcogenides *Sci. Rep.* **7** 2977

[43] Gonzales J M, Musaev D G and Morokuma K 2005 Theoretical studies of oxidative addition of E–E bonds (E = S, Se, Te) to palladium(0) and platinum(0) complexes *Organometallics* **24** 4908–14

[44] Viswanathan R *et al* 2014 Vaporization studies on elemental tellurium and selenium by Knudsen effusion mass spectrometry *J. Alloys Compd.* **603** 75–85

[45] O'Hare P A G, Lewis B M and Parkinson B A 1988 Standard molar enthalpy of formation by fluorine-combustion calorimetry of tungsten diselenide (WSe_2). Thermodynamics of the high-temperature vaporization of WSe_2. Revised value of the standard molar enthalpy of formation of molybdenite (MoS_2) *J. Chem. Thermodyn.* **20** 681–91

[46] O'Hare P A G and Hope G A 1992 Thermodynamic properties of tungsten ditelluride (WTe_2) II. Standard molar enthalpy of formation at the temperature 298.15 K *J. Chem. Thermodyn.* **24** 639–47

[47] Tonndorf P *et al* 2013 Photoluminescence emission and Raman response of monolayer MoS_2, $MoSe_2$, and WSe_2 *Opt. Express* **21** 4908

[48] Smyth C M *et al* 2018 Engineering the palladium-WSe_2 interface chemistry for field effect transistors with high performance hole contacts *ACS Appl. Nano Mater.* **2** 75–88

[49] Kim Y, Jhon Y I, Park J, Kim J H, Lee S and Jhon Y M 2016 Anomalous Raman scattering and lattice dynamics in mono- and few-layer WTe_2 *Nanoscale* **8** 2309–16